Optical trapping by petal-like circular Airy beam

Vahid Shahabadi (va.shahabadi@gmail.com)
Institute for Advanced Studies in Basic Sciences https://orcid.org/0000-0001-8792-4529
Daryoush Abdollahpour
Institute for Advanced Studies in Basic Sciences https://orcid.org/0000-0002-4149-9819

Research Article

Keywords: optical trapping, circular Airy beam, petal beam, orbital angular momentum

Posted Date: November 24th, 2020

DOI: https://doi.org/10.21203/rs.3.rs-113251/v1

Optical trapping by petal-like circular Airy beam

Vahid Shahabadi[1] **and Daryoush Abdollahpour**[1,2]

[1]Department of Physics, Institute for Advanced Studies in Basic Sciences (IASBS), Zanjan 45137-66731, Iran
[2]Optics research center, Institute for Advanced Studies in Basic Sciences (IASBS), Zanjan 45137-66731, Iran

E-mail: va.shahabadi@gmail.com

21 November 2020

Abstract. Superposition of two circular Airy vortex beams (CAVB), with opposite sign topological charges (l), produces a new type of petal beams called petal-like circular Airy beam (PCAB) with a transverse field distribution in the form of azimuthally modulated concentric rings that follow Airy function over the radial distance on a transverse plane. In this paper, tight focusing of truncated PCAB and its application in optical trapping is numerically investigated. It is shown that by adjusting the beam parameters four different trapping configurations can be achieved: a single transverse trap at a single axial position, a multi-trap geometry at a single axial position, two single transverse traps at two positions along the axial direction, and two multi-trap geometries at two different axial positions. It is also shown that the number of trapped particles in the multi-trap configurations is $2l$ per focal plane, while the number of axial trap positions is determined by the truncation aperture size. Finally, trap stiffnesses and corresponding potential energies for the trapping configurations are presented and discussed.

1. Introduction

Due to their peculiar propagation characteristics such as diffraction-free propagation, self-acceleration [1], and self-healing [2], optical Airy beams have attracted extensive attention, and rapidly drawn research interests in various applications such as filamentation [3, 4], particle clearing [5], optical micro- and nano-manipulation [6, 7], and light-sheet fluorescence microscopy [8, 9]. Several other optical beams have been designed in a way that they exhibit features of Airy beam in specific manners. Especially, beams with abrupt autofocusing property, inherited from the self-acceleration property of Airy beam, are of particular importance in several applications; circular Airy beam (CAB) [10], orbital angular momentum (OAM)-carrying circular Airy vortex beam (CAVB) [11], vector circular Airy beam (VCAB) with a cylindrically symmetric polarization distribution [12], radially polarized symmetric Airy beam [13], circular Airy beam with a Gaussian envelope [14], elliptical Airy beam [15], and Tornado waves [16] are examples of such beams. Zhu et al. have shown that the number of axial focal positions of a tight focusing CAB can be tuned by adjusting the beam parameters and the radius of a hard aperture that determines the beam extension [17]. Zhuang et al. have shown that a tightly focused CAVB has a ring-shaped transverse focal spot whose radius is determined by the topological charge (TC) of the beam [18]. Owing to their abrupt autofocusing feature, these beams have found applications in optical manipulation. There are several reports on the use of these beams in optical trapping of various particles, such as optical manipulation of Mie particles [19], optical trapping of two types of particles with lower and higher refractive indices with respect to a surrounding medium [20], trapping of Rayleigh particles [21], the formation of two axial traps by tightly focused circularly polarized CAB [22], and optical trapping and rotation of micro-particles by CAVB [23]. In 2017, Porfirev and Khonina demonstrated an azimuthally modulated circular superlinear Airy beam, as a general form of petal-like CAB [24]. The electric field envelope of the beam was considered as circular Airy function with a certain power order carrying a vortex of a certain TC, and modulated by a "circ" function. They studied the abrupt autofocusing and self-healing properties of the beam for different values of the power order and TC.

Petal-like circular Airy beams (PCABs) are a linear superposition of two CAVBs with opposite sign TCs. The transverse intensity profile of this beam is composed of azimuthally modulated petal-shaped concentric rings whose radial profile follows Airy function, while the number of petals is determined by TC. These beams also exhibit self-healing and abrupt autofocusing properties that make them a good candidate for optical micro-and nano-manipulation applications. Moreover, by adjusting the truncation aperture of the beam at an initial plane and choosing a proper TC, the geometry of three-dimensional traps formed by tightly-focused PCAB can be adjusted. In this paper, tight focusing of PCAB with different values of TC is investigated, and it is shown that by adjusting the radius of truncation aperture (aperture of the focusing lens) and other beam parameters, the focal intensity distribution can be tuned, and hence several configurations for the generated optical traps can be achieved, including a single or dual axial trap geometry with single or multiple transverse trapping sites. Generalized Lorenz-Mie theory (GLMT) is used for investigating the optical trap formation by tightly focused PCAB for sub-micron particles, and eventually, the traps are characterized in terms of their stiffness and potential energy. These findings may be found useful in the design and optimization of optical tweezers and micro-, nano-manipulation applications.

2. Theoretical approach

In this section, the formation and tight focusing of PCAB is briefly discussed, and GLMT formalism for the calculation of optical forces by using Maxwell's stress tensor is presented.

2.1. Petal-like circular Airy beam (PCAB)

Circular Airy vortex beam (CAVB) is a solution of the vector Helmholtz equation in the paraxial regime [11, 18, 23]. The electric field envelope of CAVB is given as

$$\mathbf{E}^{(l)}_{\mathrm{CAVB}}(\rho,\varphi) = E_0 \mathrm{Ai}\left(\frac{\rho_0-\rho}{w}\right)\exp\left(a\frac{\rho_0-\rho}{w}\right) \times \exp(il\varphi)\hat{\mathbf{e}}, \quad (1)$$

where E_0 is an initial amplitude, $\mathrm{Ai}(\cdot)$ denotes Airy function, ρ and φ are radial and azimuthal coordinates in a transverse plane, respectively; and ρ_0, w, a, l, and $\hat{\mathbf{e}}$ represent the radius of the first ring of the beam, a scaling factor (that determines the width of the rings), an exponential decay factor, topological charge, and polarization state, respectively.

Petal-like circular Airy beams (PCAB) are a coherent superposition of two CAVBs with identical beam parameters but opposite sign TCs. As a result, the beam will posses $2l$ main petals, and its electric field at an initial distance ($z = 0$) can be written as [24]:

$$\mathbf{E}^{(2l)}_{\mathrm{PCAB}} = \mathbf{E}^{(l)}_{\mathrm{CAVB}} + \mathbf{E}^{(-l)}_{\mathrm{CAVB}}. \quad (2)$$

Transverse intensity profiles of two PCABS with $l = 0$ and $l = 3$ are illustrated in figures 1(a) and

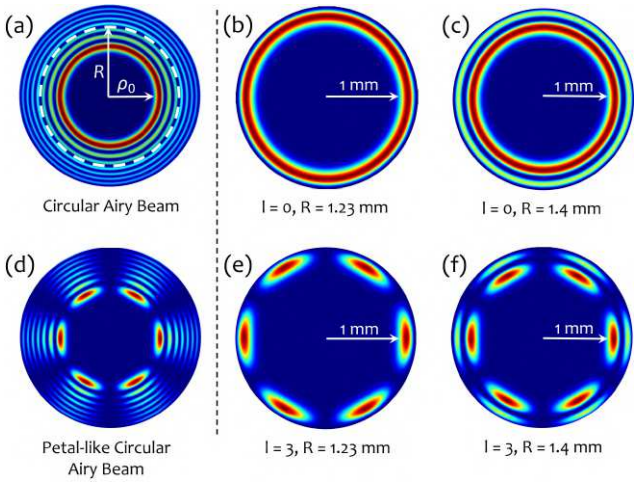

Figure 1. Transverse intensity distributions of two PCABs with $l = 0$ (a), and $l = 3$ (d). (b-f) Transverse intensity profiles of truncated PCABs with two aperture radiuses and two values of TC; (b) ($l = 0$, $R = 1.23$ mm), (c) ($l = 0$, $R = 1.4$ mm), (e) ($l = 3$, $R = 1.23$ mm), and (f) ($l = 3$, $R = 1.4$ mm).

1(d), respectively. Obviously, for $l = 0$, PCAB turns into a conventional CAB. The parameter R in figure 1 denotes the radius of the aperture of a focusing lens and determines the number of peripheral rings that are allowed to be focused by the lens while the rings with radii greater than R are truncated. Qualitatively, it can be realized that for a fixed focal length of the lens, the propagation dynamics of the focused beam, under the focusing action of the lens and abrupt autofocusing feature of the beam itself, will strongly depend on the truncation aperture R and topological charge l, for a given set of other beam parameters. Throughout this work, we investigate four combination of the choices of l and R, while other parameters are selected as $\lambda = 1064$ nm, $\rho_0 = 1$ mm, $w = 0.095$ mm and $a = 0.01$. Moreover, the beam power is set to a constant value of 100 mW in all cases.

Figures 1(b) and 1(c) show the transverse intensity profiles of a truncated PCAB with $l = 0$, for $R = 1.23$ mm and $R = 1.4$ mm, respectively. The transverse intensity profiles of PCAB with $l = 3$ and the same truncation apertures are demonstrated in figures 1(e) and 1(f), respectively. Clearly, for $R = 1.23$ mm, only the first (main) ring of the PCABs is permitted to be focused by the lens while for $R = 1.4$ mm both the main ring and a secondary ring reach the focusing lens.

2.2. Beam focusing

In the optical trapping process, the incident light beam is strongly focused to a diffraction-limited spot. According to Debye vectorial diffraction theory [25], the electric field distribution of a focused beam can be expressed as

$$\mathbf{E}_{\mathrm{f}}(r) = \mathcal{A}_0 \int_0^{\alpha} \sin\theta \int_0^{2\pi} \mathbf{E}_{\mathrm{ff,t}}(\theta,\varphi)\, e^{i\mathbf{k}\cdot\mathbf{r}} d\varphi\, d\theta, \qquad (3)$$

with

$$\mathcal{A}_0 = \left(\frac{ikfe^{-ikf}}{2\pi}\right),$$

where $k = nk_0$ is the wavenumber in the propagation medium, n is the refractive index of the medium, k_0 is the wavenumber in vacuum, f is the focal length of the lens, α is the maximum convergence angle in the medium, and (θ, φ) are the polar and azimuthal coordinates in a spherical coordinate system centered at the focus. Additionally, $\mathbf{E}_{\mathrm{ff,t}}(\theta,\varphi)$ is the transmitted far-field distribution of the electric field of the beam, given as [26]

$$\mathbf{E}_{\mathrm{ff,t}}(\theta,\varphi) = \Big(t_s(\theta)\left[\mathbf{E}^{(2l)}_{\mathrm{PCAB}}(\rho,\varphi)\cdot\hat{\boldsymbol{\varphi}}\right]\hat{\boldsymbol{\varphi}} + t_p(\theta)\left[\mathbf{E}^{(2l)}_{\mathrm{PCAB}}(\rho,\varphi)\cdot\hat{\boldsymbol{\rho}}\right]\hat{\boldsymbol{\theta}}\Big)\sqrt{\cos\theta},$$

where $t_s(\theta)$ and $t_p(\theta)$ are the Fresnel transmission coefficients of the lens for perpendicular and parallel polarization states, respectively. Here, $\hat{\boldsymbol{\rho}}$ and $\hat{\boldsymbol{\varphi}}$ are the radial and azimuthal unit vectors of a cylindrical coordinate system whose z-axis is along the propagation direction of the beam before the lens, while $\hat{\boldsymbol{\theta}}$ and $\hat{\boldsymbol{\varphi}}$, are the polar and azimuthal unit vectors of the spherical coordinate system after the lens, respectively. The calculated axial (x-z), and lateral (x-y) focal intensity distributions of the focused PCABs with several TCs ($l = 0,\ 1,\ 2,\ 3,\ 4$), and two truncation apertures of $R = 1.23$ mm and $R = 1.4$ mm, with $n = 1.33$ and $\alpha = 60°$ (i.e. NA = 1.3, for both truncation aperture sizes), are depicted in figure 2. We have assumed spherical aberration to be negligible here. As it can be seen, for $R = 1.23$ mm, and all TCs, the beam is focused in a single axial point (i.e. on a single transverse x-y plane), while for $R = 1.4$ mm, the beam forms two axial focus positions (i.e. on two xy focal planes with a longitudinal distance determined by w and f). Moreover, for $l = 0$ and both truncation apertures, the beam forms a single round focal spot in the transverse focal plane(s), while for $l \neq 0$ multiple discrete petal-shaped structures are formed in the focal plane(s), with $2l$ petals located on a circle around the optical axis (clearly noticeable for higher values of l). The diameter of the circle also depends on l and increases by increasing l. Quantitively, for $R = 1.23$ mm, the diameter of the petal-shaped structure, increases from 0.55 μm for $l = 1$ to 1.6 μm for $l = 4$. It is emphasized here that for $R = 1.4$ mm, the transverse intensity distribution is almost identical on both focal planes, which are separated by an axial distance of ~ 2.5 μm. Also, in a similar manner to the previous case, the diameter of the petal-shaped

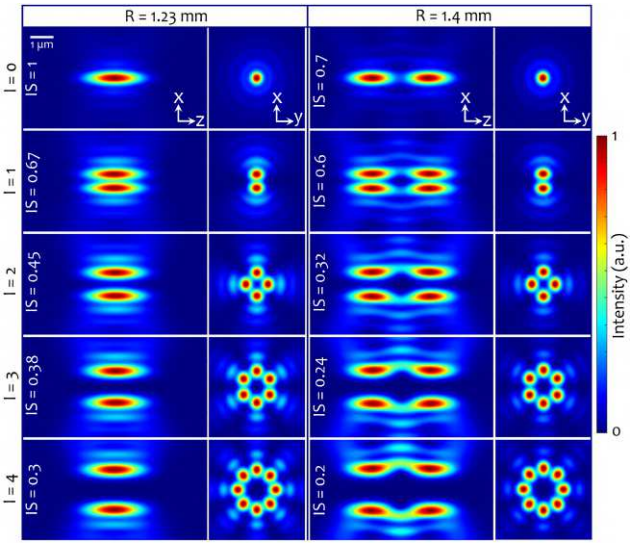

Figure 2. Longitudinal ($x-z$) and transverse ($x-y$) focal intensity distribution for $R = 1.23$, and 1.4 mm and different values of l. Depicted intensity profiles are individually normalized to their corresponding peak value for a better visual comparison of the focused beam structures. For quantitative comparison of the peak intensity for each case, the peak intensity corresponding to the case of $l = 0$ and $R = 1.23$ mm, is considered as a reference intensity scale, and the peak intensity of the depicted profiles with respect to the reference intensity scale is indicated by the intensity scale (IS) values.

structure increases from 0.57 μm for $l = 1$ to 1.7 μm for $l = 4$.

Moreover, for a better visual comparison of the focused beam structures, all intensity profiles in figure 2 are individually normalized to their corresponding peak intensity. However, for a quantitative comparison of the maximum intensity for different configurations, we considered the peak intensity achieved for $R = 1.23$ mm, and $l = 0$ as a reference intensity scale (IS). The peak intensities of the other cases, with respect to the reference intensity scale, are indicated on their focal intensity profiles. Understandably, the peak intensity is considerably reduced for the larger R and higher values of l, since the beam power is divided among multiple axial/lateral focal spots.

It should also be added that a bigger truncation aperture size, would lead to the formation of additional axial focal positions, as expected for a regular CAB [10]. However, even for a very small exponential decay factor, a, (such as the selected value of 0.01), as the radius of the peripheral rings increases, the peak intensity is reduced and the intensity contrast between the extra axial focal points, formed by those additional rings is diminished, and they eventually form a focal line. Therefore, allowing only a few first rings to form the focus would suffice for the formation of stable three-dimensional traps. Also, the effect of higher values for the exponential decay factor would be similar to the effect of a smaller truncation aperture size, with some minor differences. On the other hand, the radius of the main ring ρ_0, and its width, which is determined by the scaling factor w, determine the longitudinal, and lateral extensions of the focal region under the action of autofocusing in free space.

2.3. Optical force

Calculation of the net optical force exerted on spherical particles by a focused optical beam can be rigorously performed by using the generalized Lorenz-Mie theory (GLMT) and Maxwell's stress tensor. The first step in this procedure is the calculation of the scattered field from the particle(s) based on the GLMT. For this purpose, both the incoming and scattered electric fields are expanded in terms of electric and magnetic multipole fields [27]

$$\mathbf{E}_i = \sum_{pn'm'} \mathcal{W}^{(p)}_{n'm'} \mathbf{J}^{(p)}_{n'm'},$$
$$\mathbf{E}_s = \sum_{pn'm'} \mathcal{A}^{(p)}_{n'm'} \mathbf{H}^{(p)}_{n'm'}, \tag{4}$$

where $\mathbf{J}^{(p)}_{n'm'}$, and $\mathbf{H}^{(p)}_{n'm'}$ are the multipole fields of the incoming, and scattered electric fields, respectively, (expressed in terms of the vector spherical harmonics), $p = 1$ and $p = 2$ denote the magnetic and electric multipoles, respectively, n' determines the order of multipoles in the expansion and changes in the range of 0 to $n'_{\max}$ (that is determined by Wiscombe criterion [26]), and $m' = -n', \cdots, n'$. Finally, $\mathcal{W}^{(p)}_{n'm'}$ and $\mathcal{A}^{(p)}_{n'm'}$ are the expansion coefficients of the incoming and scattered fields, respectively. It is worth noticing that, for a spherical particle, once the expansion coefficients of the incident focused beam are found through the multipole expansion of plane waves in relation (3), the expansion coefficients of the scattered field can be obtained by using the transfer matrix of a spherical particle, as [27]

$$\mathcal{A}^{(1)}_{n'm'} = b_{n'} \mathcal{W}^{(1)}_{n'm'},$$
$$\mathcal{A}^{(2)}_{n'm'} = a_{n'} \mathcal{W}^{(2)}_{n'm'},$$

where $b_{n'}$ and $a_{n'}$ are the main diagonal elements of the transfer matrix (or the Mie coefficients) of the spherical particle and depend on the diameter, D_p, and the refractive index, n_p, of the particle.

In order to calculate the net optical force exerted on a particle, numerical integration of the time-averaged Maxwell stress tensor, $\langle \mathcal{T}_{\mathrm{M}} \rangle$, should be performed over a spherical surface (A) encircling the particle [26, 27]

$$\mathbf{F} = \int_A \langle \mathcal{T}_{\mathrm{M}} \rangle \cdot \hat{\mathbf{n}} \, ds, \tag{5}$$

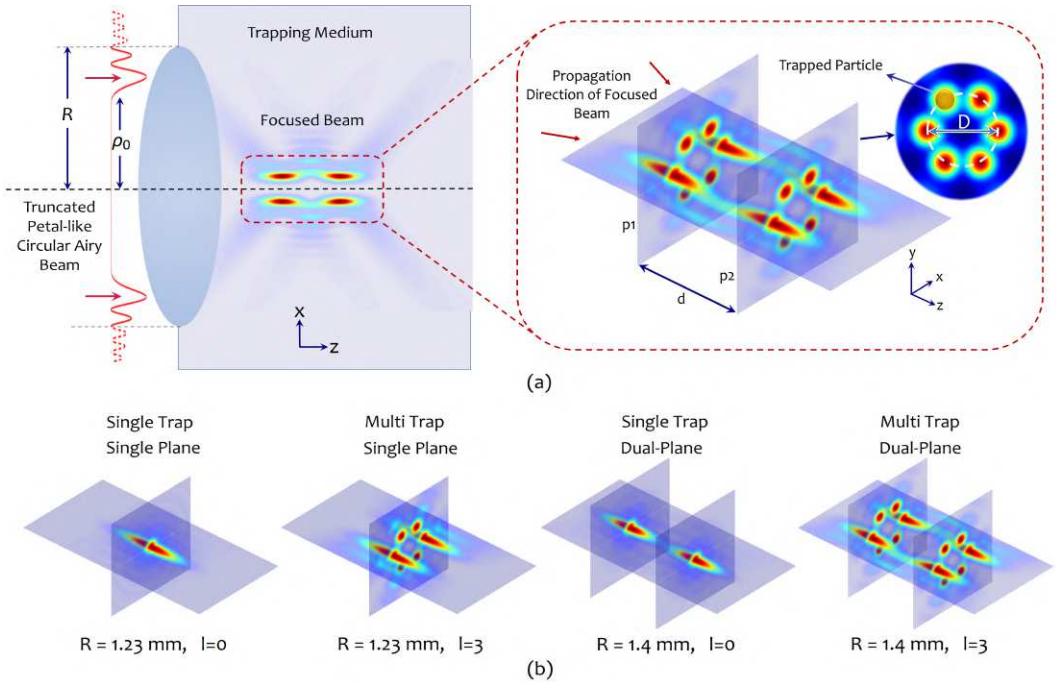

Figure 3. (a) Schematic representation of the focusing process. The truncated PCAB focuses through the lens into the trapping medium. Each particle can be trapped separately in each petal of the focused beam. Here, d is the distance between two focal planes (p1, p2) and D is the diameter of petal shape trap. (b) Depending on the truncation aperture size, R, and the value of l, four trapping configurations can be created. A single trap in a single point for $R = 1.23$ mm and $l = 0$. A multi-trap in a single plane for $R = 1.23$ mm and $l \neq 0$. Two single traps in two axial points for $R = 1.4$ mm and $l = 0$. Two multi-traps in two axial planes for $R = 1.4$ mm and $l \neq 0$.

where

$$\langle \mathcal{T}_{\mathrm{M}} \rangle = \frac{1}{8\pi} \mathrm{Re} \left\{ n^2 \mathbf{E}\mathbf{E}^* + \mathbf{B}\mathbf{B}^* - \frac{\mathbb{I}}{2}(n^2 |E|^2 + |B|^2) \right\}.$$

Here $\hat{\mathbf{n}}$ is a unit vector perpendicular to surface A; n is the refractive index of the surrounding medium, $\mathbb{I}$ is the unit dyadic, and the symbol $*$ denotes the complex conjugation. $\mathbf{B} = \mathbf{B}_i + \mathbf{B}_s$ and $\mathbf{E} = \mathbf{E}_i + \mathbf{E}_s$ are the total magnetic and electric fields, respectively, which are interrelated through $\mathbf{B} = -(i/k)\nabla \times \mathbf{E}$. Thus, the magnetic fields can be calculated when the corresponding electric fields are found using relation (4).

It is convenient to consider the optical force exerted on a trapped particle as a restoring spring force around an equilibrium position as [28]

$$F_i = -k_i \Delta i \qquad i = r, z, \tag{6}$$

where r, z, represent the lateral and axial distances from an equilibrium position, respectively, and k_i denotes the trap stiffness along each direction. Therefore, a stronger trap is expected to have greater stiffness. Additionally, following the same analogy, a potential well can be attributed to an optical trap with energy given by [29]

$$U_i = -\int_{-\infty}^{i} F_i \, di \qquad i = r, z. \tag{7}$$

A deeper potential well is associated with reduced kinetic fluctuations related to the Brownian motion of a trapped particle. The minimum depth of potential well (DPW) should be at least 10 $k_B T$ [29], where k_B is the Boltzmann constant.

3. Results and discussion

According to the mentioned theoretical description, we investigated the optical trapping of sub-micron particles under the irradiation of the focused PCABs. Throughout these investigations, the beam and focusing parameters were maintained as those described in the previous section, and the particles were assumed to be polystyrene (PS) microspheres with a diameter of $D_p = 500$ nm, and refractive index of $n_p = 1.57$ (at $\lambda = 1064$ nm).

Focusing geometry and trapping configurations of PCAB is schematically illustrated in figure 3. Depending on truncation aperture R, one or two rings of the PCAB are allowed to be focused by the lens into the trapping medium. As shown in figure 3(a), for a larger R and $l \neq 0$ (as a general case), two focal planes (p1 and p2) with a separation distance, d, are formed in the focal region. The transverse intensity distribution on each focal plane is composed

of a circular petal-shaped pattern with a diameter of D. As schematically depicted, each petal may act as an optical trap, and therefore several particles can be simultaneously trapped in such a multi-trap configuration. By the two choices of R (i.e. $R = 1.23$ mm, and $R = 1.4$ mm), and two category of options for l (i.e. $l = 0$ and $l \neq 0$), four trapping configurations can be achieved, as demonstrated in figure 3(b): a single lateral trap on a single focal plane ($R = 1.23$ mm, and $l = 0$), multiple lateral traps on a single focal plane ($R = 1.23$ mm , and $l \neq 0$), two single lateral traps on two focal planes ($R = 1.4$ mm, and $l = 0$), and finally, multiple lateral traps on two focal planes ($R = 1.4$ mm, and $l \neq 0$).

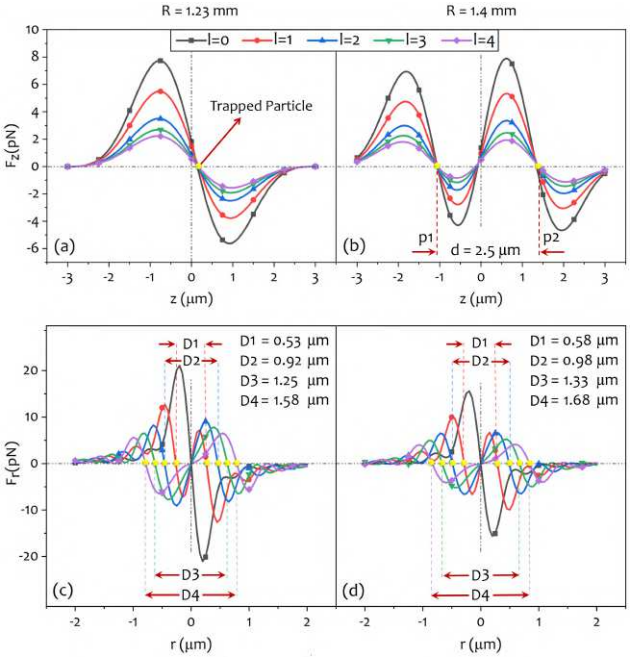

Figure 4. Diagrams of the axial (a, b), and lateral (c, d), optical forces exerted on a polystyrene microsphere with $D_p = 500$ nm, for two sizes of the truncation aperture $R = 1.23$ mm (a, c), and $R = 1.4$ mm (b, d), and several values of l. The yellow filled circles show the trap positions along the axial and lateral directions; for $l = 0$, the lateral trap position is located at $r = 0$.

The calculated axial and lateral optical forces (F_z, and F_r, respectively) exerted on PS microspheres are shown in figure 4. Clearly, for both truncation apertures, the maximum axial and lateral forces are reduced for higher values of l. This is simply due to the fact that by increasing the TC, maximum intensity on each petal of the focused beam is decreased. Moreover, it is seen that maximum lateral forces (among all cases) is higher than the maximum axial force since the beams are sharply localized along with the lateral directions than the axial direction (as it can be seen in figure 2). For instance, the maximum exerted axial force in figures 4(a) and 4(b) is about 8 pN, while in the lateral direction, the maximum exerted force is about 20 pN and 13 pN for $R = 1.23$ and 1.4 mm, respectively, as shown in figures 4(c) and 4(d).

Furthermore, it is seen that for $R = 1.23$ mm, a particle can be trapped at a single focal plane (indicated by the yellow circles in figure 4(a)), while for $R = 1.4$ mm, particle trapping may occur at any of the two focal planes (p1, and p2) as indicated by the yellow circles in figure 4(b). It should also be noted that the maximum axial forces of the single-plane and dual-plane trapping configurations are almost identical, despite the fact that the maximum intensity for $R = 1.23$ mm is higher. This can be understood based on the axial focal intensity distributions shown in figure 2; for $R = 1.23$ mm, the focus is elongated along the propagation direction, while for $R = 1.4$ mm, two discrete and rather localized focal regions are formed. This suggests that the intensity gradient is steeper for the latter case, resulting in a higher axial force.

Additionally, as depicted in figures 4(c) and 4(d), for $l \neq 0$ particle trapping may take place at different lateral positions (indicated by the yellow circles) on the petals of the focused beam whose number and geometry are determined by the value of l. It is also seen that the radial distance between the trapping positions for the single plane trapping configuration is slightly smaller than that of the dual-plane configuration. For instance, for $l = 3$ and single-plane trapping configuration, 6 particles can be trapped on a single plane with a circular geometry and a diagonal distance of 1.25 μm, whereas for $l = 3$ and dual-plane trapping configuration, 12 particles can be trapped on two focal planes (i.e. 6 particles on each plane), with a circular geometry and a diagonal distance of 1.33 μm.

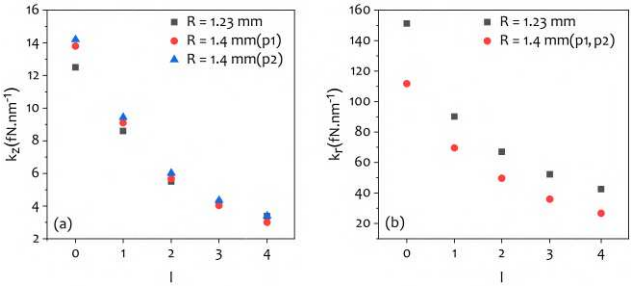

Figure 5. Calculated trap stiffnesses in (a) axial, and (b) lateral directions as a function of topological charge l, for different sizes of truncation aperture.

As stated earlier in Sec. 2, trap stiffness defined through relation (6), can be considered as a quantitative measure of the strength of an optical trap. Calculated stiffnesses for the optical traps indicated in figure 4 in both axial and lateral directions for various trapping configurations are plotted in figure

5. Obviously, the lateral trap stiffnesses are about an order of magnitude higher than the axial ones. Also, figure 5(a) shows that for $l = 0$ dual-plane trapping configuration has a higher trap stiffness than a single-plane configuration. This is due to smaller and rather localized focal spots along the axial direction in the former case. Additionally, by increasing the value of the TC, trap stiffness is decreased from ~ 14 fN.nm^{-1}, for $l = 0$, to ~ 3 fN.nm^{-1}, for $l = 4$. On the other hand, in the lateral direction, as shown in figure 5(b) the single-plane trapping configuration forms stronger traps for all values of l due to slightly smaller spot sizes, and higher peak intensities on each petal on the focal plane. Here, the calculated lateral stiffnesses for the dual-plane case are the same on both focal planes, p1, and p2.

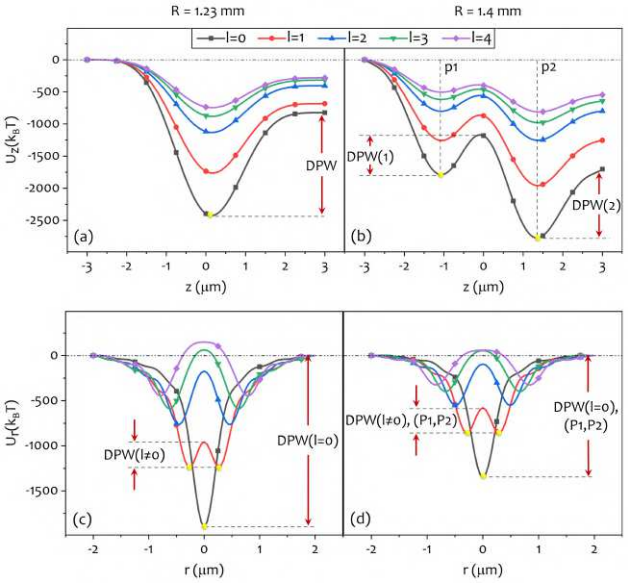

Figure 6. Calculated potential energy of the optical traps and their corresponding depth of potential well (DPW), for different configurations. (a) and (b) show the potential energy diagram for $R = 1.23$ mm, and $R = 1.4$ mm, respectively, in axial direction, while (c) and (d) show the corresponding diagrams in lateral direction.

Moreover, relation (7) was used to calculate the potential energy of the optical traps. The calculated potential energies along axial and lateral directions are shown in figure 6 (T = 300 K is selected in this study). Figures 6(a) and 6(b) show the axial potential energy for the single-, and dual-plane trapping configurations, respectively. It is seen that depth of potential well (DPW), defined as the energy difference between a local minimum and a nearest local maximum, is in general, greater for single-plane configuration than a dual-plane one since in the latter case the beam power is divided into two focal regions (i.e. planes), between at least two focal spots, each on an individual focal plane. For instance, for $l = 0$, DPW in the single-plane configuration is about 1500 k_BT, while the corresponding values in the dual-plane configuration are about 600 k_BT, and 1100 k_BT, on p1 and p2, respectively. The least DPW is achieved for $l = 4$ in the first focal plane of the dual-plane configuration, with a value of 125 k_BT; however, this value is still well beyond the minimum DPW required for the formation of a stable trap (10 k_BT). The lateral potential energies are shown in figures 6(c) and 6(d) for single- and dual-plane trapping configurations, respectively. Obviously, in both cases, single transverse traps ($l = 0$) provide greater DPW than the multiple traps ($l \neq 0$); and higher l is associated with a further reduced DPW. Also, a comparison of figures 6(c) and 6(d) reveals that the lateral DPW is lower for the dual-plane trapping case. These are attributed to the power division between two focal planes in the case of dual-plane trapping, and further reduction of the peak intensity in each trapping site by increasing the value of l. Furthermore, it is important to note here, when the diagonal distance (D) between multiple trapping sites is comparable to the particle diameter (D_p), multiple transverse potential wells are converted to a single potential well, in a way that the multi-petal beam structure acts equivalently as a single large spot, and hence a single trap is formed with reduced DPW. In our case, $D_p = 0.5$ μm, while the minimum diagonal distance between trapping sites of $D = 0.53$ μm is achieved for $l = 1$ with two petals. This indicates that the two particles can almost independently be trapped in each petal with a reduced DPW; however, higher values of l are associated with larger diagonal distances, and therefore DPW has increased again for $l > 1$. On the other hand, a perfect $2l$ multiple trap configuration for a petal beam with the topological charge of l can only be achieved when the particle diameter does not exceed the distance between two adjacent petals, as it is ensured here.

4. Conclusion

In summary, it was shown that a superposition of two circular Airy vortex beams (CAVBs), with opposite sign topological charge, produces a new kind of optical beams called petal-like circular Airy beam (PCAB) that is promising for applications such as optical manipulation. Tight focusing of PCAB for two truncation apertures (R) and several values of the topological charge (l) is numerically investigated, and it is shown that different combinations of these parameters result in different intensity distributions around the focal region. It is demonstrated that four distinct trapping configurations can be achieved by proper choices of the parameters: (i) A single lateral trap on a single focal plane ($R = 1.23$ mm and $l = 0$);

(ii) A petal-shape lateral multiple-trap geometry on a single focal plane ($R = 1.23$ mm, and $l \neq 0$); (iii) Two single lateral traps on two distinct focal planes ($R = 1.4$ mm, and $l = 0$); and (iv) Two petal-shape lateral multiple-trap geometries on two distinct focal planes ($R = 1.4$ mm, and $l \neq 0$). The trap stiffness (k) and the depth of potential well (DPW), for each case, is calculated, and it is discussed that a perfect $2l$ lateral multiple-trap geometry can be achieved for particle size smaller than the distance between adjacent trap sites. The work may find applications in the implementation of particle trapping, and nano-, micro-manipulation by PCAB and similar azimuthally modulated, abruptly autofocusing beams.

Competing interests

The authors declare no competing interests.

References

[1] Siviloglou G, Broky J, Dogariu A and Christodoulides D 2007 *Physical Review Letters* **99** 213901
[2] Broky J, Siviloglou G A, Dogariu A and Christodoulides D N 2008 *Optics express* **16** 12880–12891
[3] Polynkin P, Kolesik M, Moloney J V, Siviloglou G A and Christodoulides D N 2009 *Science* **324** 229–232
[4] Abdollahpour D, Suntsov S, Papazoglou D G and Tzortzakis S 2010 *Physical review letters* **105** 253901
[5] Baumgartl J, Mazilu M and Dholakia K 2008 *Nature photonics* **2** 675–678
[6] Zhao Z, Zang W and Tian J 2016 *Journal of Optics* **18** 025607
[7] Cheng H, Zang W, Zhou W and Tian J 2010 *Optics express* **18** 20384–20394
[8] Vettenburg T, Dalgarno H I, Nylk J, Coll-Lladó C, Ferrier D E, Čižmár T, Gunn-Moore F J and Dholakia K 2014 *Nature methods* **11** 541–544
[9] Kafian H, Lalenejad M, Moradi-Mehr S, Birgani S A and Abdollahpour D 2020 *Scientific Reports* **10** 1–12
[10] Papazoglou D G, Efremidis N K, Christodoulides D N and Tzortzakis S 2011 *Optics letters* **36** 1842–1844
[11] Kadlimatti R and Parimi P V 2018 *IEEE Transactions on Antennas and Propagation* **67** 260–269
[12] Wang F, Zhao C, Dong Y, Dong Y and Cai Y 2014 *Applied Physics B* **117** 905–913
[13] Xu C, Hu H, Liu Y and Deng D 2020 *Optics Letters* **45** 1451–1454
[14] Geng T and Zhang X 2020 *Optics Express* **28** 2447–2455
[15] Zha Y, Huang K, Liu B, Sun M, Hu H, Li N, Zhang X, Zhu B and Lu X 2018 *Applied optics* **57** 6717–6720
[16] Brimis A, Makris K G and Papazoglou D G 2020 *Optics Letters* **45** 280–283
[17] Zhu W and She W 2015 *Optics Communications* **334** 303–307
[18] Zhuang J, Zhang L and Deng D 2020 *Optics Letters* **45** 296–299
[19] Lu W, Sun X, Chen H, Liu S and Lin Z 2019 *Physical Review A* **99** 013817
[20] Jiang Y, Cao Z, Shao H, Zheng W, Zeng B and Lu X 2016 *Optics Express* **24** 18072–18081
[21] Sun M, Zhang J, Li N, Huang K, Hu H, Zhang X and Lu X 2019 *Optics express* **27** 27777–27785
[22] Chen Z and Jiang Y 2020 *Journal of Quantitative Spectroscopy and Radiative Transfer* **244** 106851
[23] Chen M, Huang S, Liu X, Chen Y and Shao W 2019 *Applied Physics B* **125** 184
[24] Porfirev A P and Khonina S N 2017 *JOSA B* **34** 2544–2549
[25] Richards B and Wolf E 1959 *Proceedings of the Royal Society of London. Series A. Mathematical and Physical Sciences* **253** 358–379
[26] Jones P H, Maragò O M and Volpe G 2015 *Optical tweezers: Principles and applications* (Cambridge University Press)
[27] Borghese F, Denti P, Saija R and Iati M A 2007 *Optics Express* **15** 11984–11998
[28] Rohrbach A 2005 *Physical Review Letters* **95** 168102
[29] Wang L, Cao Y, Zhu T, Feng R, Sun F and Ding W 2017 *Optics Express* **25** 29761–29768

Figures

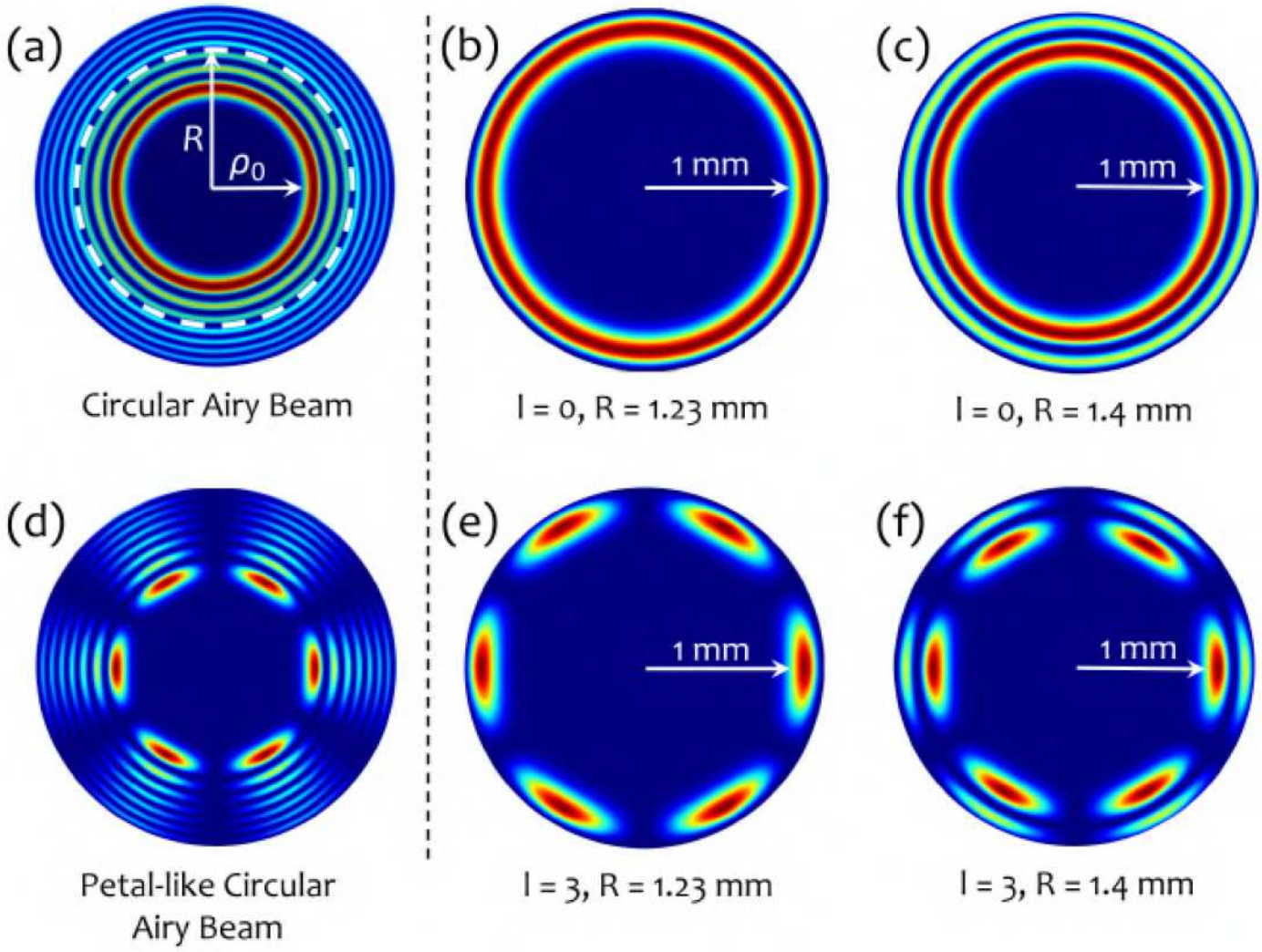

Figure 1

Transverse intensity distributions of two PCABs with l = 0 (a), and l = 3 (d). (b-f) Transverse intensity proles of truncated PCABs with two aperture radiuses and two values of TC; (b) (l = 0, R = 1:23 mm), (c) (l = 0, R = 1:4 mm), (e) (l = 3, R = 1:23 mm), and (f) (l = 3, R = 1:4 mm).

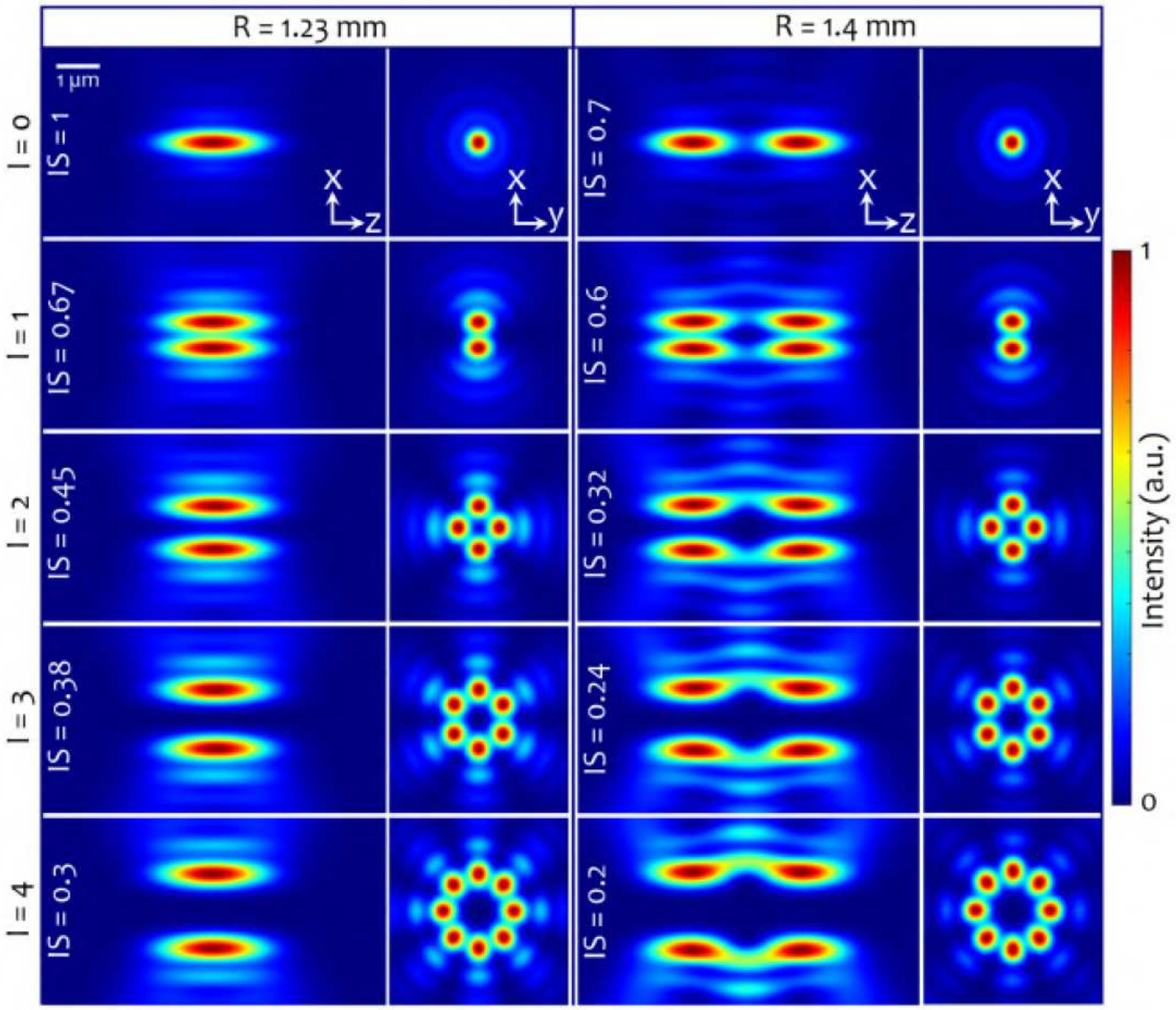

Figure 2

Longitudinal (x − z) and transverse (x − y) focal intensity distribution for R = 1.23, and 1.4 mm and different values of l. Depicted intensity profiles are individually normalized to their corresponding peak value for a better visual comparison of the focused beam structures. For quantitative comparison of the peak intensity for each case, the peak intensity corresponding to the case of l = 0 and R = 1.23 mm, is considered as a reference intensity scale, and the peak intensity of the depicted profiles with respect to the reference intensity scale is indicated by the intensity scale (IS) values.

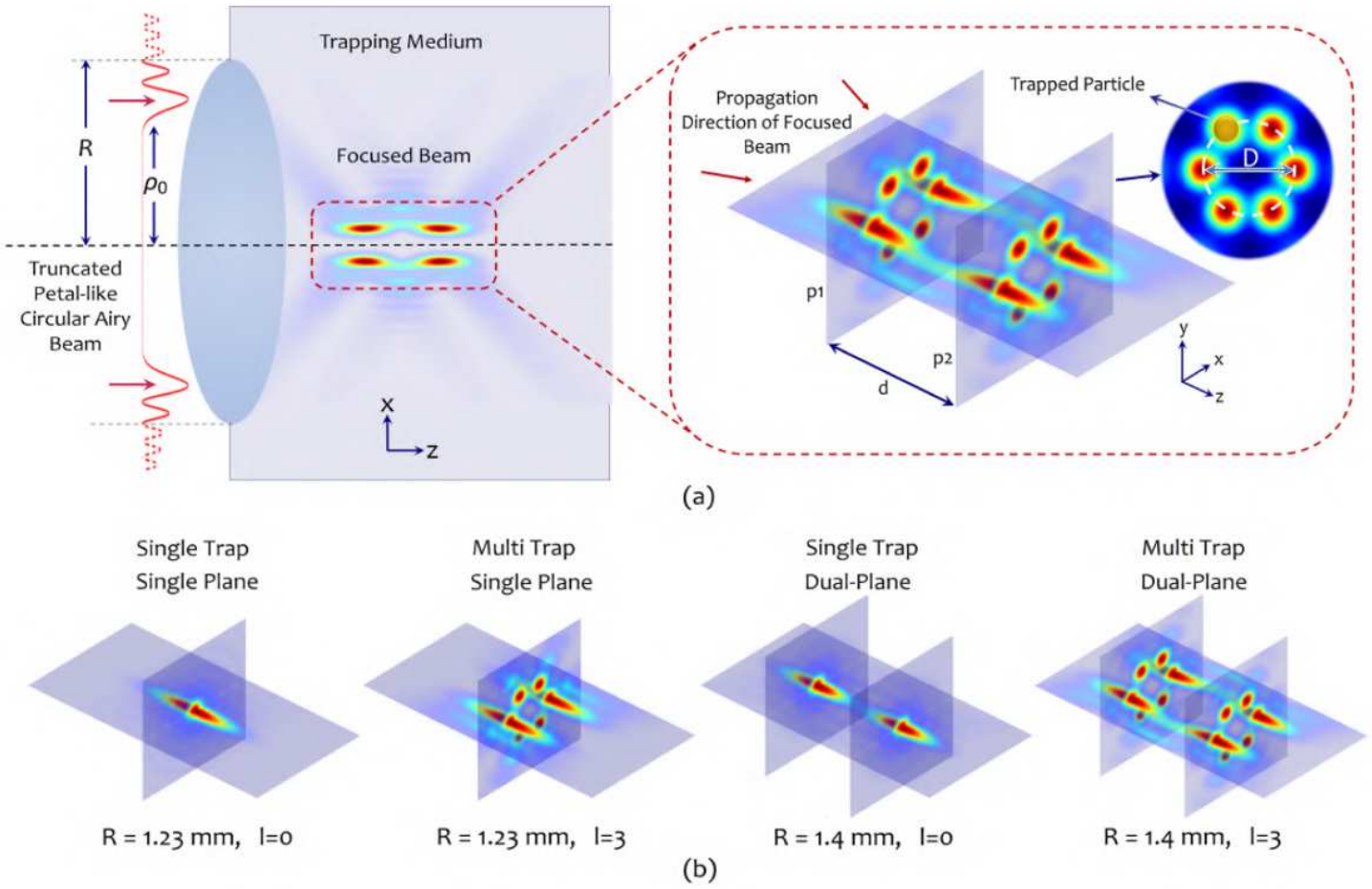

Figure 3

(a) Schematic representation of the focusing process. The truncated PCAB focuses through the lens into the trapping medium. Each particle can be trapped separately in each petal of the focused beam. Here, d is the distance between two focal planes (p1, p2) and D is the diameter of petal shape trap. (b) Depending on the truncation aperture size, R, and the value of l, four trapping configurations can be created. A single trap in a single point for R = 1.23 mm and l = 0. A multi-trap in a single plane for R = 1.23 mm and l ≠ 0. Two single traps in two axial points for R = 1.4 mm and l = 0. Two multi-traps in two axial planes for R = 1.4 mm and l ≠ 0.

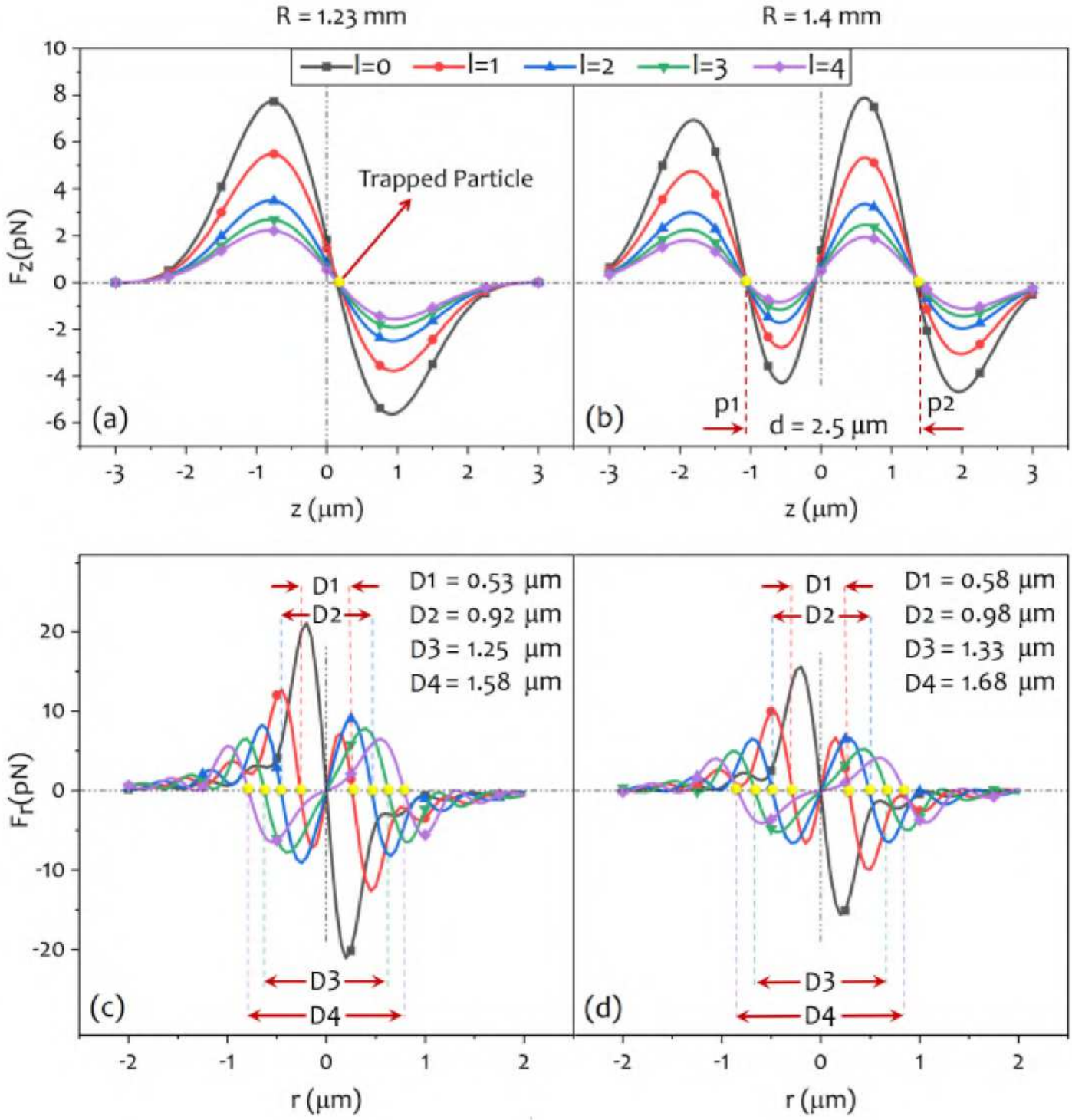

Figure 4

Diagrams of the axial (a, b), and lateral (c, d), optical forces exerted on a polystyrene microsphere with Dp = 500 nm, for two sizes of the truncation aperture R = 1.23 mm (a, c), and R = 1.4 mm (b, d), and several values of l. The yellow filled circles show the trap positions along the axial and lateral directions; for l = 0, the lateral trap position is located at r = 0.

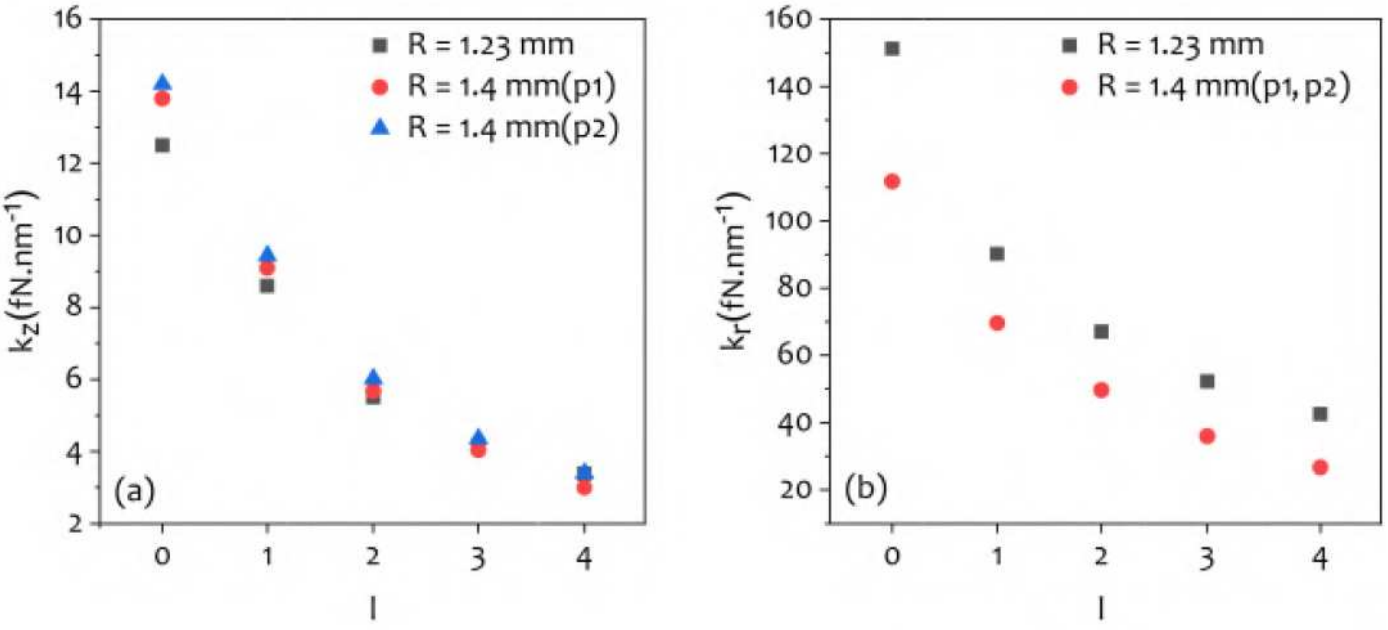

Figure 5

Calculated trap stiffnesses in (a) axial, and (b) lateral directions as a function of topological charge l, for different sizes of truncation aperture.

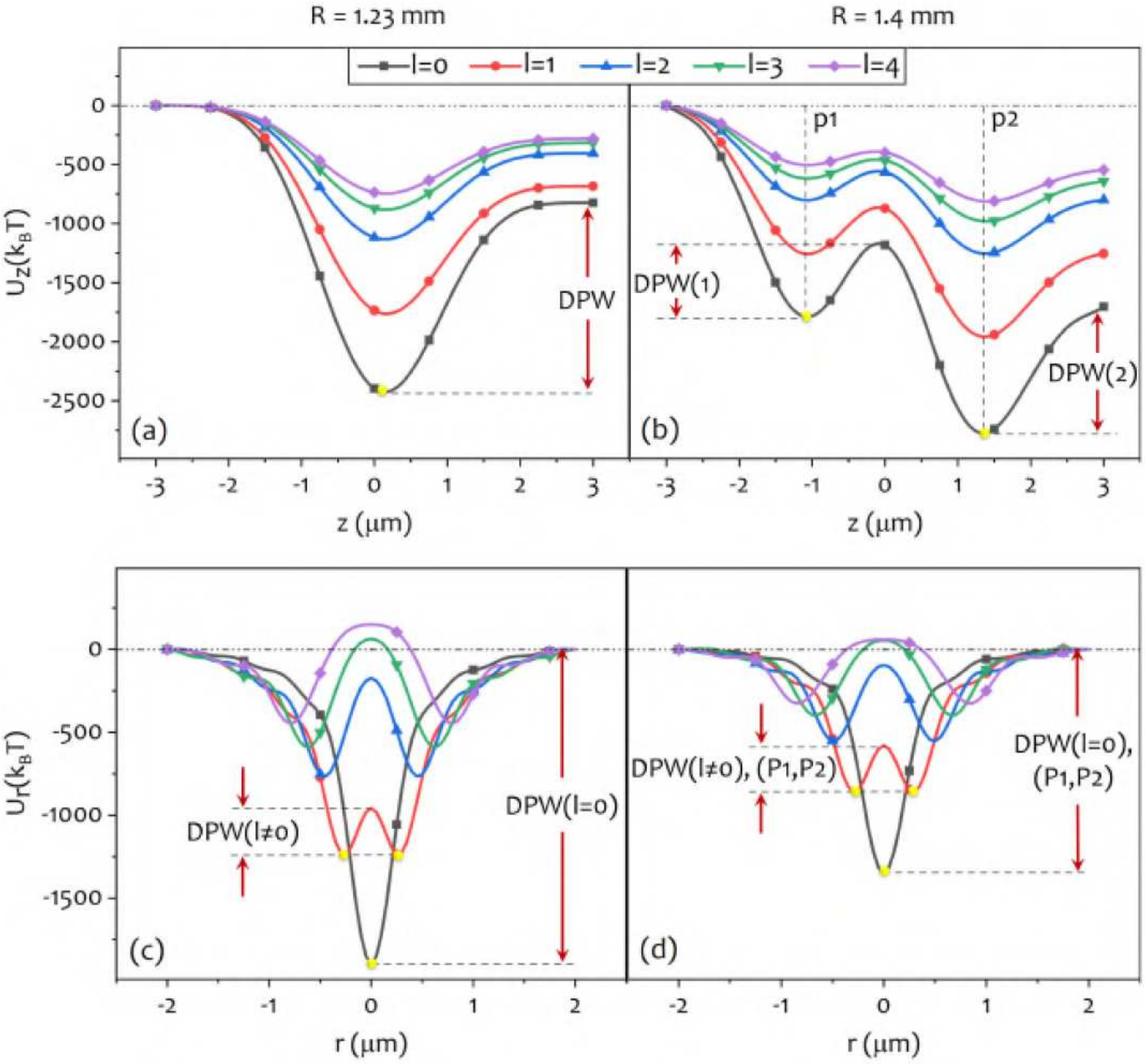

Figure 6

Calculated potential energy of the optical traps and their corresponding depth of potential well (DPW), for different configurations. (a) and (b) show the potential energy diagram for R = 1.23 mm, and R = 1.4 mm, respectively, in axial direction, while (c) and (d) show the corresponding diagrams in lateral direction.